Separation and Purification Technology 378 (2025) 134695

Contents lists available at ScienceDirect

Separation and Purification Technology

journal homepage: www.elsevier.com/locate/seppur

Recycling and utilization of cobalt, nickel, and manganese from black mass of spent Li-Ion batteries for supercapacitor applications

Oğuzhan Onar [a], Sezgin Yasa [b,*], Ozan Aydin [a], Burak Birol [a], Metin Gencten [a,c]

[a] Yildiz Technical University, Faculty of Chemical and Metallurgical Engineering, Department of Metallurgy and Materials Engineering, 34210 Istanbul, Turkey
[b] Cankiri Karatekin University, Faculty of Engineering, Department of Mechanical Engineering, Cankiri, Turkey
[c] İstinye University, Faculty of Engineering and Natural Sciences, 34396 İstanbul, Turkey

ARTICLE INFO

Editor: Rajiv R. Srivastava

Keywords:
Spent Li-ion battery black mass
Cobalt oxide
Nickel oxide
Manganese oxide supercapacitor

ABSTRACT

In this study, a supercapacitor cathode electrode material was produced by recycling the black mass from spent Li-ion batteries, utilizing nickel, cobalt, and manganese compounds recovered from the recycling process. During the leaching process of the black mass powder, H_2SO_4 and a fixed 10 vol% H_2O_2 solution were used as the leaching medium. The effects of different acid molarities and leaching durations on the leaching efficiency were investigated. Cobalt/nickel/manganese hydroxide (CNMOH) and cobalt/nickel/manganese oxide (CNMO) were synthesized through conversion and used as cathode electrode materials in asymmetric supercapacitors. The areal capacitance values of CNMOH and CNMO electrodes were determined as 1219 mF/cm^2 and 333 mF/cm^2 at a scan rate of 5 mV/s in three elecrode system. The areal and spesific capacitance of the CNMOH//G coin-cell asymmetric supercapacitor at a scan rate of 5 mV/s were determined to be 252 mF/cm^2 and 50.8 F/g respectively. The areal and spesific capacitance of the CNMO//G coin-cell asymmetric supercapacitor were also found as 223.17 mF/cm^2 and 50 F/g respectively. Additionally, at a current density of 1 mA/cm^2, the energy density of 7 Wh/kg and power density of 334.35 W/kg for CNMO//G supercapacitor and the energy density of 8.78 Wh/kg and power density of 263.09 W/kg for CNMOH//G supercapacitor were calculated. After 10,000 cycles, both CNMOH//G and CNMO//G supercapacitors retained more than 100 % of their initial capacitance.

1. Introduction

In today's world, people's dependence on energy is increasing day by day. Due to the rising demand for energy resources, energy storage systems have become a crucial issue alongside energy production. Therefore, electrochemical batteries and electrochemical capacitors (supercapacitors) are of critical importance in this regard [1]. Lithium-ion batteries (LIBs) have become one of the most widely used energy storage systems in daily life [2]. The increasing use of LIBs in recent years has resulted in the generation of large quantities of waste batteries. Consequently, the recycling of critical metals from these waste LIBs has become an essential area of research [3].

LIBs can be classified based on their cathode composition, including types such as $LiCoO_2$ (LCO), $LiMn_2O_4$ (LMO), Li(Ni-Mn-Co)O_2 (NMC), Li(Ni-Co-Al)O_2 (NCA), and $LiFePO_4$ (LFP) [3–5]. Among these, lithium-nickel-manganese-cobalt oxide ($LiNixMnyCozO_2$), commonly referred to as NMC, is considered one of the most advanced technologies today [6]. NMC-type LIBs are further categorized based on their transition metal composition, including variants such as $LiNi_{1/3}Co_{1/3}Mn_{1/3}O_2$ (NMC111), $LiNi_{0.5}Co_{0.2}Mn_{0.3}O_2$ (NMC523), $LiNi_{0.6}Co_{0.2}Mn_{0.2}O_2$ (NMC622), and $LiNi_{0.8}Co_{0.1}Mn_{0.1}O_2$ (NMC811). Each transition metal plays a specific role: Ni enhances specific capacity, Co contributes to cycle stability, and Mn improves structural integrity. Compared to $LiCoO_2$-based LIBs, NMC-type LIBs offer several advantages, including high recyclability, lower cost, and environmental benefits. Additionally, Ni is the primary redox-active element influencing the electrochemical capacity of NMC [7].

With an estimated 1 million tons of LIBs expected to reach end-of-life by 2030, effective recycling strategies are essential to minimize landfill waste and recover valuable raw materials. Consequently, LIB recycling has become mandatory, and this industrial process must be conducted sustainably. NMC cathodes are widely used in electric vehicles (EVs), and their composition is continuously evolving. However, as the volume of spent batteries grows exponentially, the demand for sustainable recycling technologies also increases. Industrial NMC recycling is primarily performed using pyrometallurgical and hydrometallurgical

* Corresponding author.
E-mail address: sezginyasa@karatekin.edu.tr (S. Yasa).

https://doi.org/10.1016/j.seppur.2025.134695
Received 8 April 2025; Received in revised form 28 July 2025; Accepted 7 August 2025
Available online 8 August 2025
1383-5866/© 2025 Elsevier B.V. All rights are reserved, including those for text and data mining, AI training, and similar technologies.

Table 1
Sample codes and compositions of the prepared positive electrodes for supercapacitors.

Supercapacitor codes	CNMO	CNMOH	Carbon Black	PVDF
CNMO//G	%80	–	%10	%10
CNMOH//G	–	%80	%10	%10

processes or a combination of both [8]. In many hydrometallurgical studies, H_2O_2 has been used as a reducing agent along with acids such as H_2SO_4 and HCl [9–14]. This approach facilitates the reduction of Co^{3+} to Co^{2+} and Mn^{4+} to Mn^{2+}, enhancing the dissolution of these metals [11,15]. The precipitation of Co, Ni, and Mn as hydroxides is largely completed at pH 10 and above in alkaline media [12].

Transition metals such as Ni, Co, and Mn, which exhibit multiple valence states, possess several easily ionizable electrons in their electronic configurations, resulting in excellent electrochemical performance [16]. Transition metal-based electrode materials offer high energy densities, superior specific capacitances, and rapid charge/discharge rates [17]. Several studies have explored the use of recycled NMC materials in supercapacitor applications. Choi et al. hydrometallurgically recycled NMC-type LIBs and precipitated $NiMnCoC_2O_4$ using oxalic acid. The resulting material was used as an electrode in a supercapacitor, achieving a capacitance of 1641 F/g in a three-electrode system on nickel foam, with 80 % retention of initial capacitance after 4000 cycles Another study synthesized LiNiMnCo-oxide from hydrometallurgically recovered NMC and incorporated it into a supercapacitor [18]. In a system where C76-modified LiNiMnCo-oxide was used as the positive electrode and graphene as the negative electrode, a specific capacitance of 30 F/g was obtained at 1 A/g current density [9]. Similarly, another study precipitated NiMnCo-oxalate during NMC battery recycling and used it as a supercapacitor electrode. In a device using activated carbon as the negative electrode and mixed metal oxalate as the positive electrode, a specific capacitance of 89.5 F/g was achieved at 0.5 A/g current density. The device retained 74 % of its initial capacitance after 5000 cycles [10]. A review of the literature indicates that research on supercapacitors produced from recycled NMC-type LIBs is still limited, with most studies published in 2022 and 2023, making it a highly relevant topic. A comprehensive study in this area would provide significant contributions to both academic research and industrial applications. Additionally, previous studies have focused on cobalt sulfide and cobalt oxide/hydroxide recovered from LCO-type LIBs for use in supercapacitors [19–22]. However, research on metal oxide/hydroxide-based supercapacitors derived from recycled NMC-type LIBs remains scarce, highlighting the need for further investigation. This study is important both in determining the effectiveness of hydrometallurgical processes for Li-ion battery recycling and in determining the effectiveness of the hydroxide and oxide compounds formed by cobalt, nickel and manganese from these recycling products as supercapacitor electrode materials.

In this study, a comprehensive approach was undertaken, starting from black mass recycling, followed by leaching and precipitation processes, and culminating in the supercapacitor application of the recycled materials.

2. Experimental

2.1. Leaching and precipitation

The spent Li-ion battery used in this study was supplied as black mass by Exitcom. The composition of the black mass was determined using XRF analysis. Before the experiments, To remove small amounts of metals such as iron, aluminum and copper in the black mass, the black mass was pretreated by mixing it in a 0.5 M H_2SO_4 solution for 1 min. After drying, the leaching processes were initiated with the black mass powder. Initially, three separate leaching solutions were prepared using 1 M concentrations of H_2SO_4, HNO_3 and HCl each containing 10 vol% H_2O_2 (30 %). Leaching was performed in these solutions at a solid-to-liquid ratio of 1:50 for 2 h. Subsequently, further leaching experiments were conducted using only H_2SO_4. The effect of acid concentration on leaching efficiency was investigated in solutions containing 0.5–3 M H_2SO_4 with a constant 10 vol% H_2O_2. To examine the effect of the solid-to-liquid ratio on leaching efficiency, experiments were conducted for 2 h in solutions containing 3 M H_2SO_4 and 10 vol% H_2O_2 at solid-to-liquid ratios of 1:10, 1:20, 1:40, and 1:50. Additionally, the effect of leaching time on efficiency was investigated in solutions with a fixed composition of 3 M H_2SO_4 and 10 vol% H_2O_2 at a solid-to-liquid ratio of 1:50. All leaching processes were carried out at room temperature without additional heating. The leachate obtained after 2 h in 3 M H_2SO_4 with 10 vol% H_2O_2 was filtered, and the precipitation process was performed by adjusting the pH of the solution to approximately 10 using NaOH (99 %) solution. The precipitated material was then calcined at 500 °C to obtain the oxide form of the compound. All chemicals used in the experiments were of analytical or technical grade.

2.2. Characterization of CNMOH and CNMO

The cobalt/nickel/manganese hydroxide (CNMOH) and cobalt/nickel/manganese oxide (CNMO) powders were characterized using X-ray diffraction (XRD), Fourier transform infrared spectroscopy (FT-IR), and field emission scanning electron microscopy (FE-SEM). Additionally, the CNMOH powder was analyzed using thermogravimetric analysis and differential thermal analysis (TG/DTA). TG/DTA analysis (Hitachi Exstar, SII TG/DTA 7300) was conducted to examine phase transitions and mass changes with increasing temperature. Surface morphology observations and elemental analysis of CNMOH and CNMO were performed using a Carl Zeiss Sigma 300 VP FE-SEM device. Phase analysis of CNMOH and CNMO was carried out using an X-ray diffractometer (Malvern PANalytical, Cu Kα radiation). FT-IR analysis was conducted with a Bruker Tensor II spectrometer to identify functional groups in the powders. SPECS Surface Nano Analysis GmbH and Thermo Scientific K-Alpha device was used for X-ray photoelectron spectroscopy (XPS) analysis.

2.3. Electrode preperation and electrochemical characterization of CNMOH//G and CNMO//G supercapacitors

For the preparation of three-electrode system and two-electrode coin cell-type asymmetric supercapacitors, graphite foil was used as the current collector. In addition to CNMOH and CNMO, 10 % carbon black and 10 % polyvinylidene fluoride (PVDF) were used as binders in the cathode composition. Two different electrode compositions were prepared: (1) CNMOH, carbon black, and PVDF in an 8:1:1 mass ratio, and (2) CNMO, carbon black, and PVDF in the same 8:1:1 mass ratio. The electrode compositions are summarized in Table 1. The prepared mixtures were dispersed in N-Methyl-2-pyrrolidone (NMP, 99.5 %, Chemsolute) as a solvent and coated onto graphite foil using the Doctor Blade method with a film applicator. The coated films were then dried in an oven at 90 °C for 12 h. The negative electrode composition was prepared using nano graphite with 10 % by mass PVDF as a binder and NMP as a solvent. In the three-electrode system, Graphite, CNMOH and CNMO were used as working electrodes. Platinum electrode and Ag/AgCl were used as the counter electrode and reference electrode, respectively. In the contruction of coin cell type symmetric supercapacitor, the electrodes were cut into 16 mm diameter discs. Positive and negative electrodes were separated using a Whatman separator, and asymmetric supercapacitors were assembled using a battery crimping device with 6 M KOH (85 %) as the electrolyte. The active substance ratios (negative/positive) between the positive electrode and the negative electrode were measured to be approximately 2.5 for CNMOH//G and 3 for CNMO//G.

The electrochemical characterization of the fabricated supercapacitors was conducted using cyclic voltammetry (CV), GCD, and

Table 2
XRF analyses of black mass powder.

Black mass ingredients	Co_3O_4	NiO	MnO	CuO	Fe_2O_3	Al_2O_3
Compounds (weight)	63.013 %	22.11 %	7.899 %	5.349 %	1.454 %	0.175 %
Black mass ingredients	Co	Ni	Mn	Cu	Fe	Al
Atomic(weight)	60.4 %	23.84 %	8.37 %	5.84 %	1.39 %	0.13 %

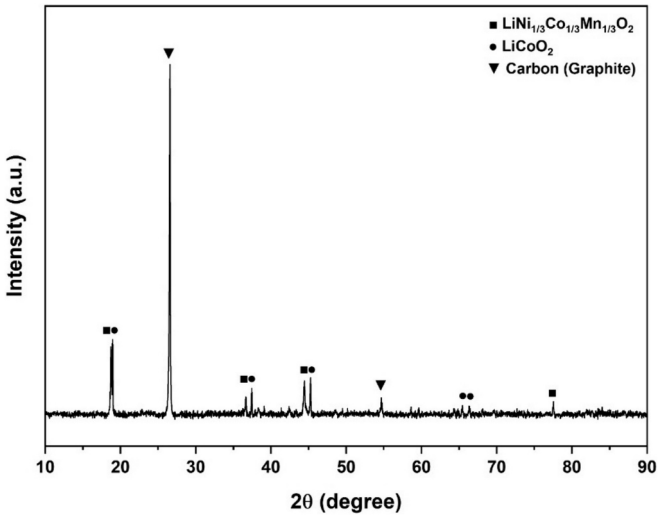


Fig. 1. XRD pattern of black mass powder, showing the presence of Carbon, LCO, and NMC cathode materials.

electrochemical impedance spectroscopy (EIS) tests with a Gamry potentiostat/galvanostat. Potential range optimizations were performed at a scan rate of 50 mV/s, within potential ranges of 0–1 V, 0–1.2 V, 0–1.4 V, and 0–1.6 V. Cyclic voltammograms were recorded at scan rates ranging from 5 mV/s to 500 mV/s. GCD tests were conducted at varying current densities, and long-term cycle stability tests were performed over 10,000 cycles using GCD. Specific capacitance and areal capacitance were calculated from CV data according to the equations in Eq. (1) and Eq. (2), respectively. In these equations, V, v, s, and a represent the potential range, scan rate, weight of the active material on the cathode electrode, and the area of the cathode electrode, respectively [23–25].

$$\text{Specific capacitance} = \int \frac{IdV}{\Delta V \times v \times s} \tag{1}$$

$$\text{Areal capacitance} = \int \frac{IdV}{\Delta V \times v \times a} \tag{2}$$

The energy density (E) and power density (P) of CCTAS were calculated using Eq. (3) and Eq. (4). In these equations, Δt, Δv, C, represent the discharge time, potential range and specific capacitance, respectively [26,27].

$$E = \frac{C^*(\Delta V)^2}{2} \tag{3}$$

$$P = \frac{E}{\Delta t} \tag{4}$$

3. Results and discussion

3.1. Characterization of black mass

The carbon content of the black mass was determined by calcination of the black mass powder at 1000 °C for 3 h, yielding a carbon content of 49.3 %. XRF analysis was conducted directly on the black mass, and the results, showing the composition percentage of the remaining 50.7 %, are provided in Table 2. Upon evaluating the results, it is inferred that the copper in the black mass likely originates from the current collector in the anode section. Additionally, the very small amount of aluminum is likely to come from the cathode section in the batteries.

XRD analysis was performed on the black mass powder to determine the types of Li-ion battery cathode materials contained in the supplied black mass. According to the results of the XRD analysis (Fig. 1), it was determined that the structure of the black mass contained a significant amount of Carbon (Reference Code: 01-089-8487) [28], LCO (Reference Code: 00-016-0427)[29] and and NMC (Reference Code: 98-008-6131) type cathode materials.

3.2. Leaching and precipitation of black mass

Leaching experiments were carried out with the powder obtained after washing the black mass with 0.5 M H_2SO_4 for 1 min. Firstly, leaching experiments were carried out with different acids to determine the most suitable acid for leaching processes. For this purpose, separate leaching experiments were carried out for 2 h with HCl, H_2SO_4 and HNO_3 acids containing 1 M and 10 vol% H_2O_2 and the results are shown in Fig. 2a. According to these results, it was determined that the solubility of cobalt, nickel and manganese in black mass did not change much with the acid type and leaching experiments were continued with H_2SO_4. Fig. 2b shows the effect of different solid/liquid ratios on solubility. All leaching experiments here were performed with 3 M H_2SO_4 containing 10 % H_2O_2 by volume for 2 h. It was determined that the best solubility was achieved when the solid/liquid ratio was 1/50. An initial decrease in leaching efficiency, followed by an increase, was observed with the increase in the solid/liquid ratio. To explain this phenomenon, it is essential to consider the role of carbon present in the black mass during the leaching process. Black mass is rich in carbon, which can play a significant role in adsorbing metal ions during the leaching process [30]. Initially, as the solid/liquid ratio increases, the amount of solid material in the mixture increases, reducing the efficiency of the acid solution in dissolving the metal ions. In this case, the carbon in the black mass, due to its surface characteristics and porous structure, can adsorb metal ions, which negatively affects the leaching efficiency. That is, as the solid content increases, the available surface area for dissolution may be limited, and the adsorptive properties of carbon can hinder the release of metal ions into the solution. However, beyond a certain point, further increases in the solid/liquid ratio result in more efficient dissolution. At this stage, the presence of a sufficient amount of acidic solution facilitates the transfer of metal ions into the solution, and the negative effects of carbon's adsorption capacity begin to diminish. Therefore, while the increase in the solid/liquid ratio initially leads to a decrease in efficiency due to adsorption, after reaching a certain equilibrium point, leaching efficiency improves. Fig. 2c shows the effect of molarity of H_2SO_4 on solubility in different acid solutions containing constant 10 % H_2O_2 in solid/liquid ratio of 1/50. From 0.5 M to 3 M, Co, Ni and Mn solubility increased continuously and reached a maximum point at 3 M. Fig. 2d shows the effect of time on the solubility of Co, Ni and Mn in leaching experiments carried out at solid/liquid ratio of 1/50 in 3 M H_2SO_4 acid concentration containing 10 % H_2O_2. In the leaching experiments from 15 to 120 min, the maximum leaching efficiency was reached in 120 min. After leaching, the precipitation process was carried out by using NaOH solution to bring the pH to around 10. Then, after the filtration process, the washing process was carried out several times with pure water and finally the CNMOH material was dried in the oven. The

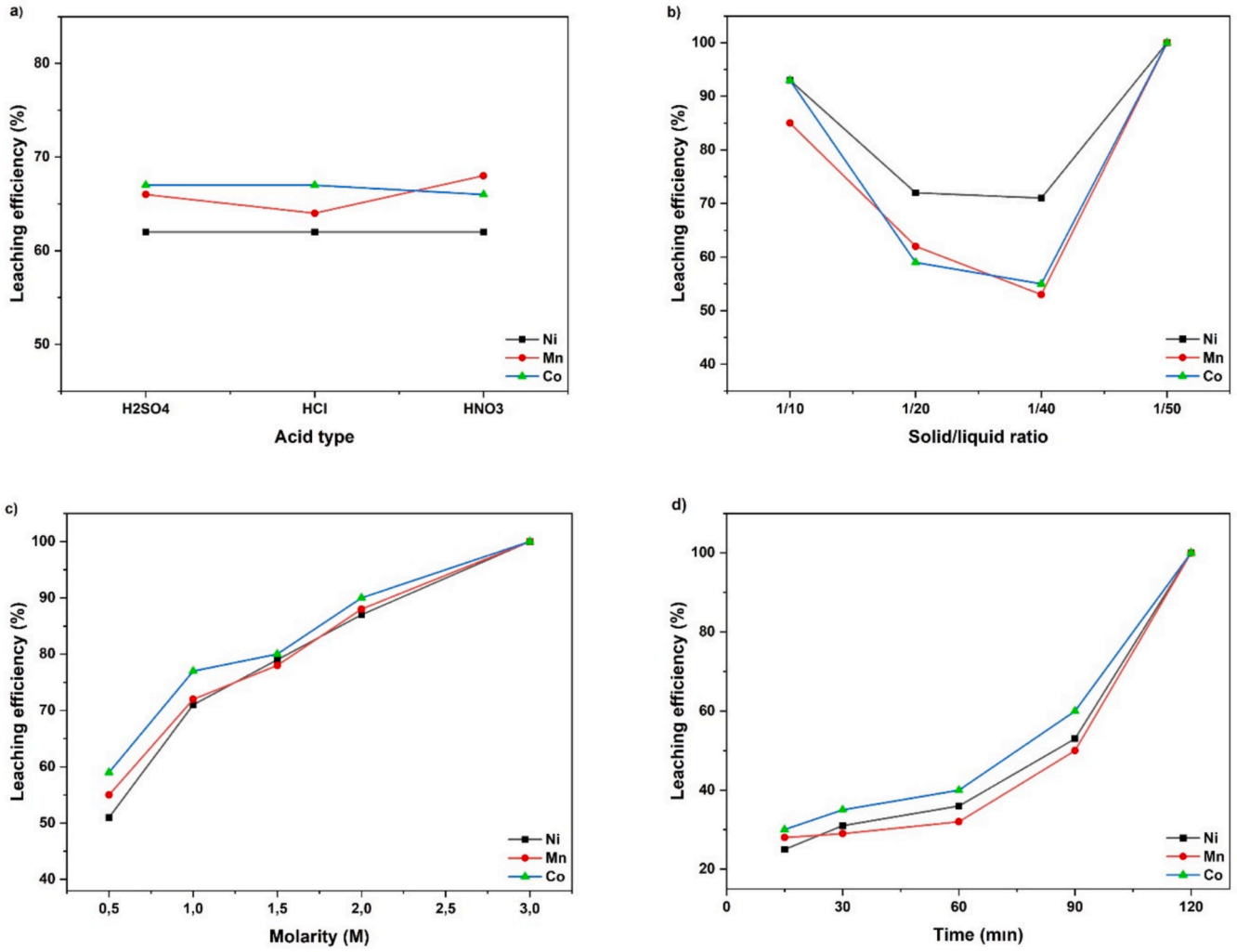


Fig. 2. Effect of different parameters on leaching efficiency: a) acid type, b) solid/liquid ratio, c) molarity, d) time.

use of strong acids in the leaching process and the precipitation process in a basic environment is an cost effective method in Li-ion battery recycling, but its negative effects in terms of the environment should also be evaluated. In this study, the effect of the acid was eliminated by bringing the pH to around 10 and as a result, the remaining filtered liquid solution became basic. In addition, it is possible to minimize the environmental impact by neutralizing the waste basic solution.

3.3. *Characterization of CNMOH and CNMO*

The microstructural and elemental analyses of both CNMOH and CNMO powders were performed using Field Emission Scanning Electron Microscopy (FE-SEM), and the results for CNMOH powder are presented in Fig. 3 a-f. FE-SEM images at different magnifications seen in Fig. 3 a-d show that the particles are in micron and nano sizes and also that there is some agglomeration. The elemental analysis of CNMOH powder reveals the presence of cobalt (Co), nickel (Ni), manganese (Mn), and oxygen (O) (Fig. 3e). The elemental mapping images, provided in Fig. 3e, confirm that the distribution of these elements is homogeneous throughout the material. In Fig. 3f, the composition of these elements is shown in terms of both weight and atomic percentages. These observations suggest a uniform incorporation of the metals within the structure, which is essential for ensuring consistent electrochemical performance in supercapacitor applications.

The microstructural and elemental analyses of CNMO powder are presented in Fig. 4a–f. When Fig. 4a–d is examined, FE-SEM images taken at different magnifications show that there is no partial sintering during the calcination process. Similar to CNMOH powder, the CNMO powder is composed of cobalt (Co), nickel (Ni), manganese (Mn), and oxygen (O) elements, which are uniformly distributed throughout the structure. A comparison of Fig. 3f and Fig. 4f reveals that the oxygen content in CNMOH is higher than that in CNMO. This is due to the presence of metal hydroxide compounds, specifically in the form of $M(OH)_2$, in CNMOH, whereas CNMO consists primarily of metal oxides, which contain less oxygen. This difference in oxygen content can significantly influence the electrochemical behavior of these materials in supercapacitor applications. The higher oxygen content in CNMOH can contribute to improved pseudocapacitance facilitating better charge and ion transport, thus enhancing the overall energy storage performance of supercapacitors. Oxygen defects and structures with oxygen vacancies are known to enhance pseudocapacitive behavior. For instance, the presence of oxygen defects is associated with improved electrochemical properties due to increased active sites and enhanced ion diffusion rates, as seen in materials like nickel/cobalt molybdate and tin oxide engineered with oxygen-deficient interfaces [31,32].

Additionally, some studies indicate that structural modifications resulting in higher oxygen content or oxygen vacancies can significantly boost the pseudocapacitive properties of electrode materials. This has been demonstrated in similar systems where the electrochemical performance is enhanced by the engineered oxygen vacancies, leading to more available and accessible charge storage sites that are crucial for pseudocapacitive energy storage [33]. The homogenous distribution of

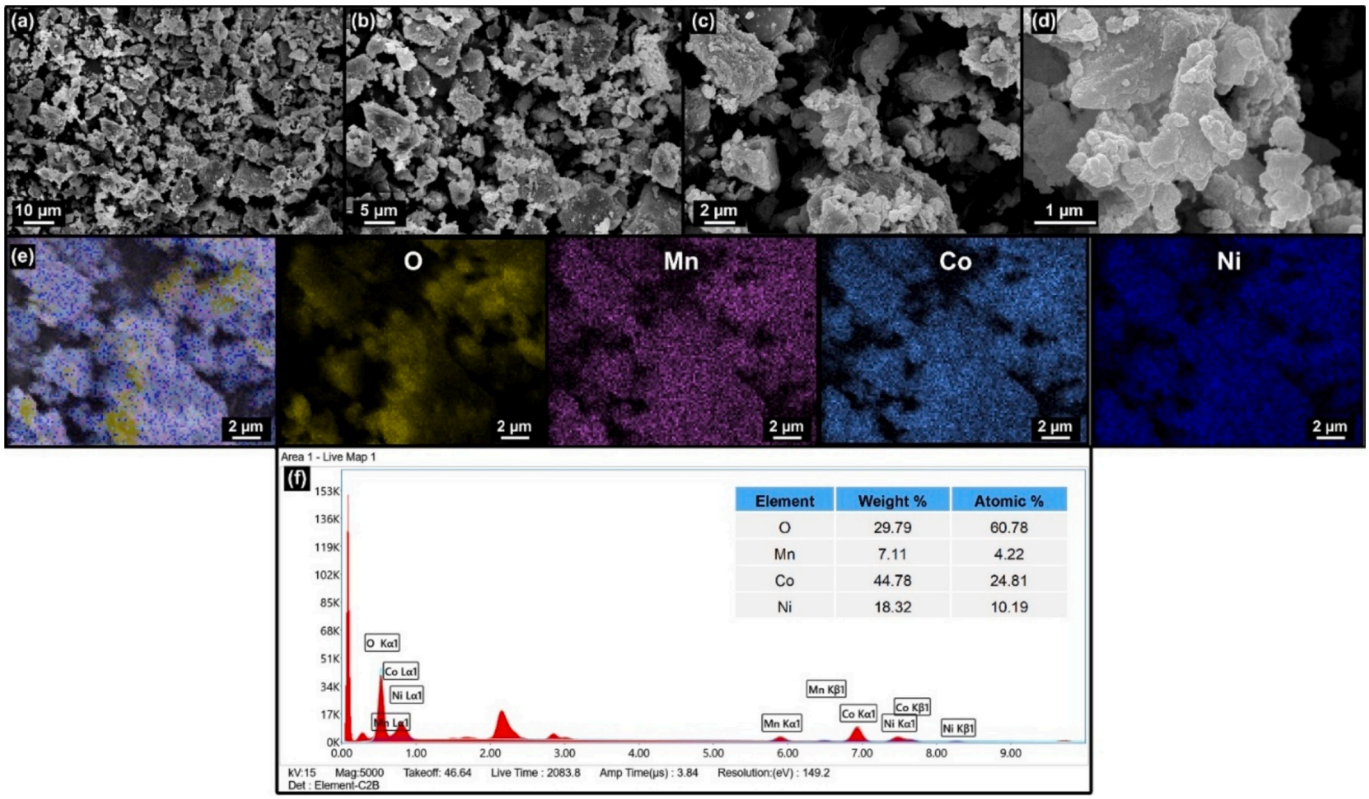


Fig. 3. FE-SEM images and elemental analysis of CNMOH powder: a) 1000x, b) 2000x, c) 5000x d) 10000x e) Elemental mapping of O, Mn, Co, and Ni, f) Weight and atomic percentage composition of the elements.

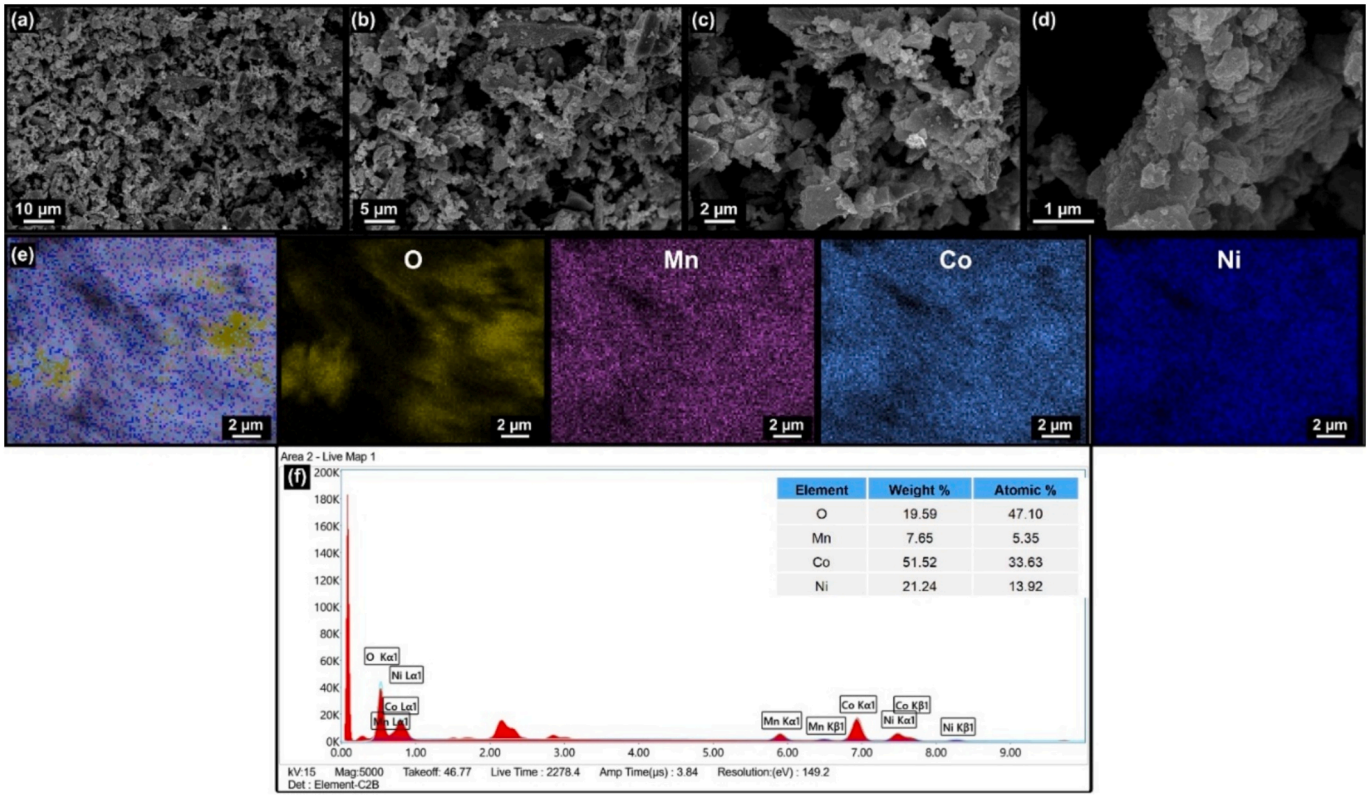


Fig. 4. FE-SEM images and elemental analysis of CNMO powder: a) 1000x, b) 2000x, c) 5000x d) 10000x e) Elemental mapping of O, Mn, Co, and Ni, f) Weight and atomic percentage composition of the elements.

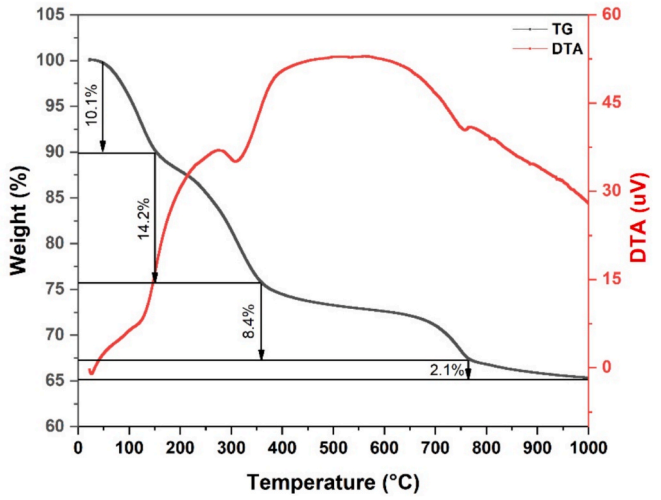


Fig. 5. Thermogram of TG/DTA analysis of CNMOH powder.

elements in both CNMOH and CNMO powders plays a crucial role in maintaining consistent electrochemical performance, ensuring stable charge–discharge cycles and high cycling efficiency in supercapacitor applications.

TG/DTA analysis provides information about the mass loss due to reactions that occur with increasing temperature in the CNMOH material obtained by the precipitation process (Fig. 5). Initially, the mass decrease up to about 150 °C is likely due to the evaporation of physical water. Subsequently, a significant mass loss (approximately 14.2 %) occurs between 150 °C and 400 °C. The endothermic peak observed between 300 and 400 °C can be attributed to the formation of the oxide form of metal hydroxides [34]. This endothermic behavior in this temperature range indicates that metal hydroxides tend to convert into oxides as they are heated, leading to a loss in mass. These transformations are important reactions that can affect the material's properties, especially in electrochemical applications [33].

The chemical composition and crystalline structure of the synthesized material were determined using XRD analysis [19]. The XRD pattern of the produced CNMOH and CNMO materials are shown in Fig. 6(a–b). The diffraction peaks in Fig. 6a correspond to $Co(OH)_2$ (Reference Code: 01-089-8616) [35], $Ni(OH)_2{\cdot}0.75H_2O$ (Reference Code: 00-038-0715) [36], and $Mn(OH)_2$ (Reference Code: 00-008-0171) [37]. The diffraction peaks of CNMO in Fig. 6b are attributed to Co_3O_4 (Reference Code: 00-001-1152) [38], NiO_2 (Reference Code: 01-085-1977) [39], and Mn_3O_4 (Reference Code: 00-001-1127) [40]. These results confirm that the hydroxide and oxide structures of cobalt, nickel, and manganese were successfully synthesized.

Fig. 7 presents the FT-IR spectra of CNMO and CNMOH powders. The prominent absorption band at 435 cm^{-1} corresponds to the metal–oxygen stretching vibrations, specifically the Ni–O bond, and the vibration of manganese species (Mn^{3+}) in an octahedral coordination site [41,42]. Absorption peaks between 500–800 cm^{-1} are attributed to the vibrations of metallic M−O and M−OH groups, including those of Ni, Mn, and Co [43]. The peaks at 543 cm^{-1} and 532 cm^{-1} are associated with Co–O stretching vibrations [44]. A peak at 640 cm^{-1} can be assigned to Ni=O stretching [45], as well as the vibration of Mn^{3+} species in an octahedral site [42], and the Co–O absorption band [46]. The peak at 1056 cm^{-1} likely reflects a structural transformation, corresponding to the formation of NiO nanoparticles from $Ni(OH)_2$ [47]. Additionally, the bending mode of adsorbed water is clearly represented by a peak at 1634 cm^{-1}, while the broad band observed in the range of 3250–3500 cm^{-1} is characteristic of the O–H stretching vibrations of hydroxyl groups on the oxide surface [48].

XPS survey spectra of CNMOH and spectra of Co 2p, Ni 2p, Mn 2p and O1s fitted using the gaussian model are shown in Fig. S1 and Fig. 8a–d, respectively. The main peaks at binding energies of 781.74 eV and 798.30 eV are attributed to Co $2p_{3/2}$ and Co $2p_{1/2}$, respectively. These peaks and satellite peak at binding energy of 786.14 eV show the

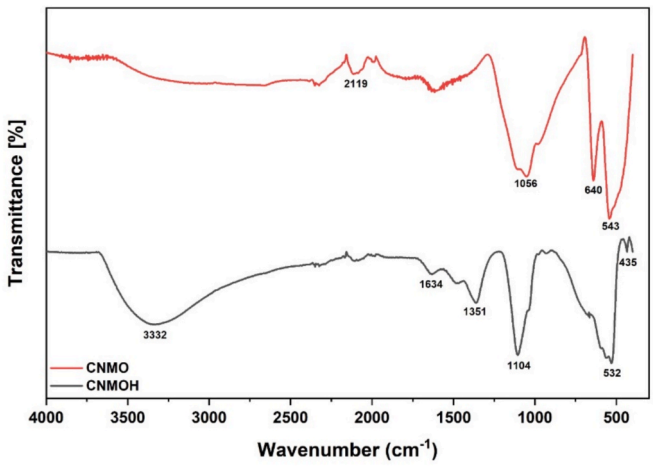


Fig. 7. FT-IR spectra of CNMO and CNMOH powders.

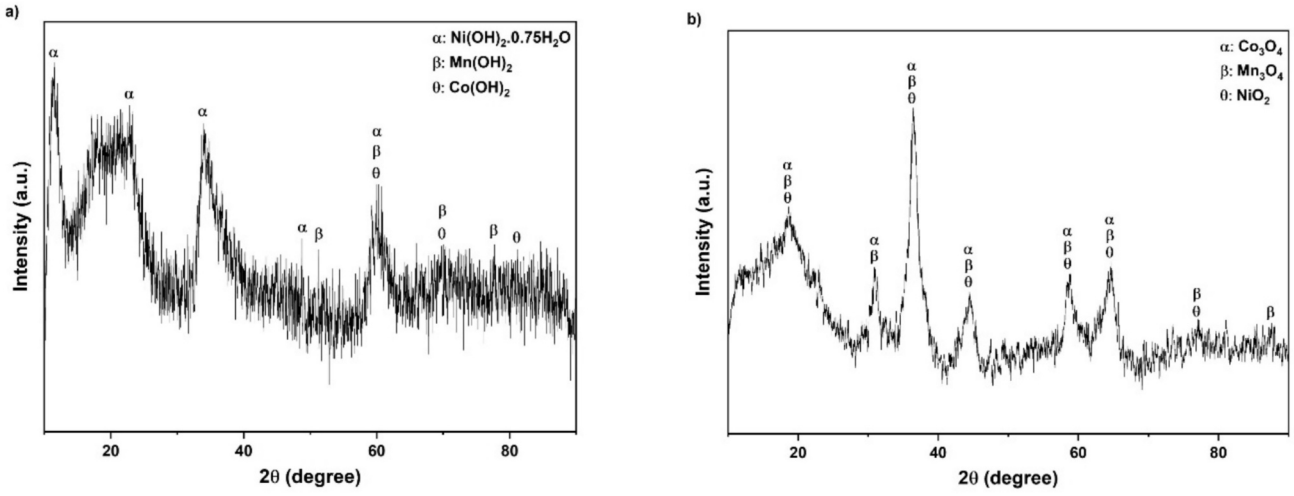


Fig. 6. a) XRD pattern of CNMOH powder and b) XRD pattern of CNMO powder.

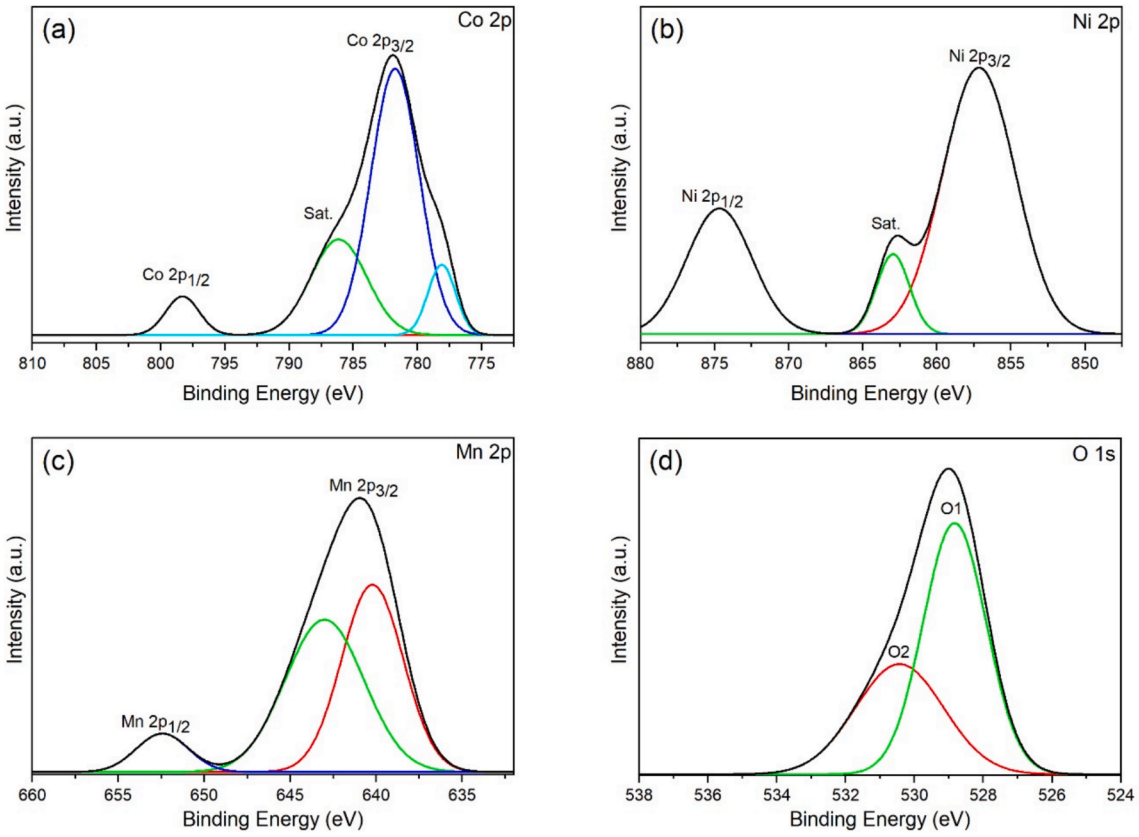


Fig. 8. XPS spectra of CNMOH a) Co 2p, b) Ni 2p, c) Mn 2p and d) O1s.

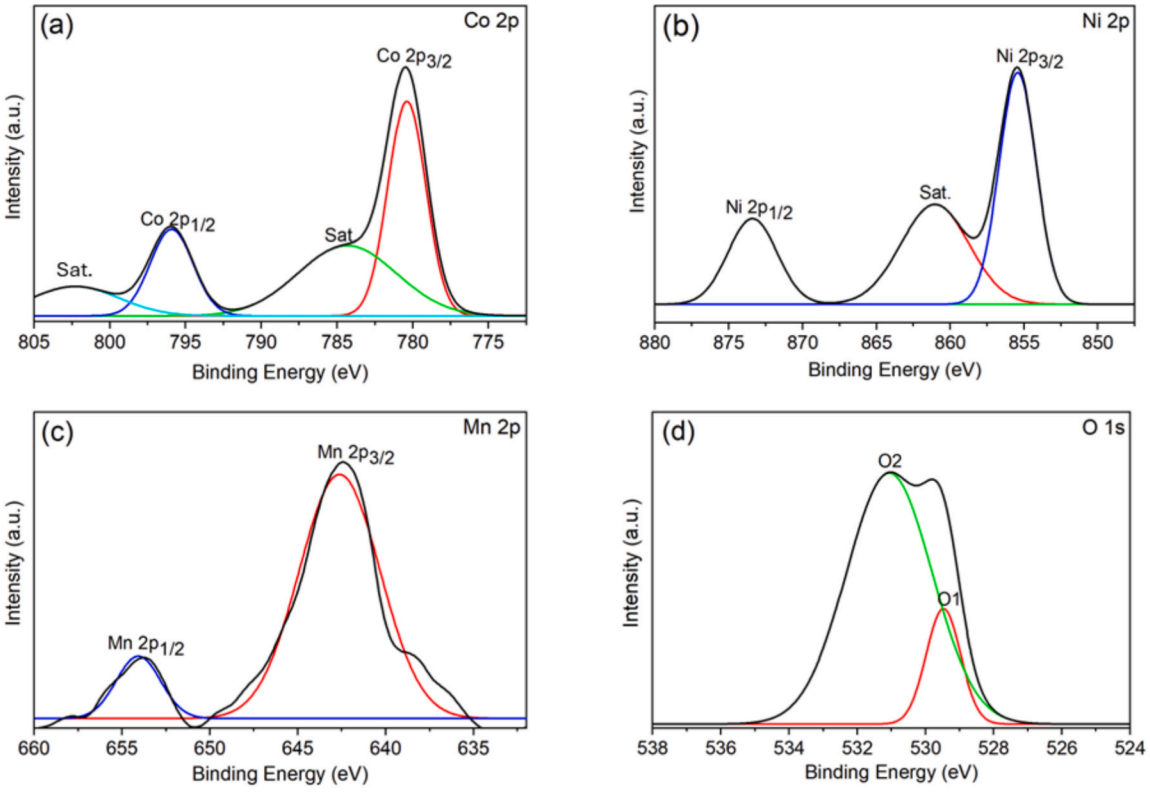


Fig. 9. XPS spectra of CNMO a) Co 2p, b) Ni 2p, c) Mn 2p and d) O1s.

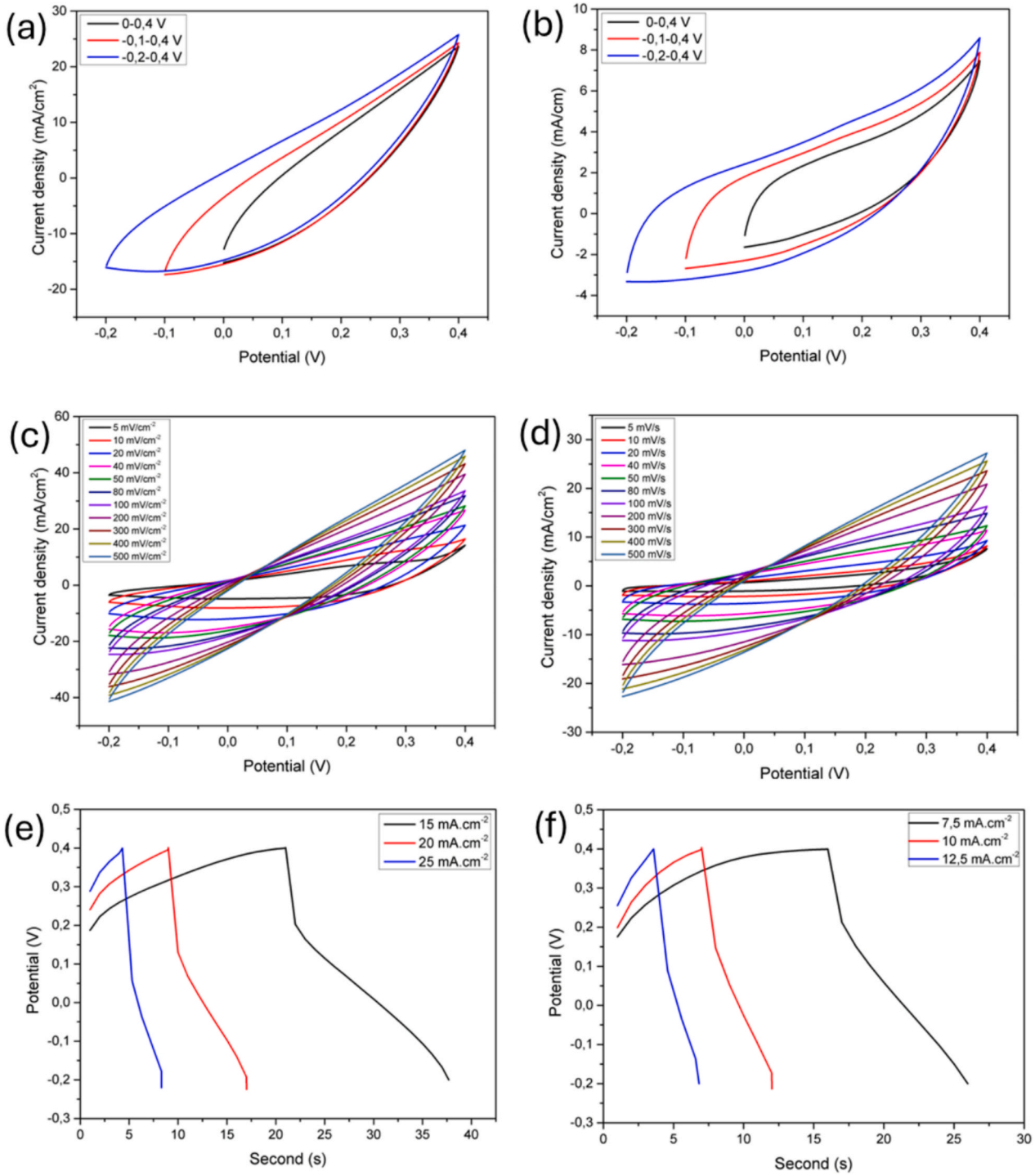


Fig. 10. a) Optimization of the potential range for the CNMOH supercapacitor, b) Optimization of the potential range for the CNMO supercapacitor, c) Cyclic voltammograms of the CNMOH supercapacitor at different scan rates, d) Cyclic voltammograms of the CNMO supercapacitor at different scan rates, e) GDC test of CNMOH supercapacitor and f) GDC test of CNMO supercapacitor.

chemical state of Co^{2+} in $Co(OH)_2$ (Fig. 8a) [49]. The peaks at binding energies of 857.16 eV and 874,68 eV in the Fig. 8b are assigned to the $Ni^{2+}2p_{3/2}$ and $Ni^{2+}2p_{1/2}$, respectively [50]. Main peaks of $Mn(OH)_2$ around 640.22 eV and 652.43 eV are characteristic for Mn $2P_{3/2}$ and Mn $2P_{1/2}$, respectively (Fig. 8c) [51]. Peaks at binding enegies of 528.83 eV (O1) and 530.44 eV (O2), which are ascribed to lattice O^{2-} species and surface hydroxide OH^{-}, respectively, are shown in Fig. 8d [52].

XPS survey spectra of CNMO and spectra of Co 2p, Ni 2p, Mn 2p and O1s fitted using the gaussian model are shown in Fig. S2 and Fig. 9a-d, respectively. Co 2p XPS spectrum of Co_3O_4 is demonstrated in Fig. 9a and peaks at binding energies of 780.4 and 795.9 are assigned to Co $2p_{3/2}$ and Co $2p_{1/2}$, respectively [53]. The peaks at binding energies of 855.43 eV (Ni^{+3}) and 873,4eV (Ni^{+2}) in the Fig. 9b are assigned to the $Ni2p_{3/2}$ and $Ni2p_{1/2}$, respectively [54]. Main peaks of MnO around 642.62 eV and 654.07 eV are characteristic for Mn $2P_{3/2}$ and Mn $2P_{1/2}$, respectively (Fig. 9c) [55]. Peaks at binding enegies of 529.48 eV (O1) and 531.06 eV (O2), which are ascribed to metal–oxygen bond and

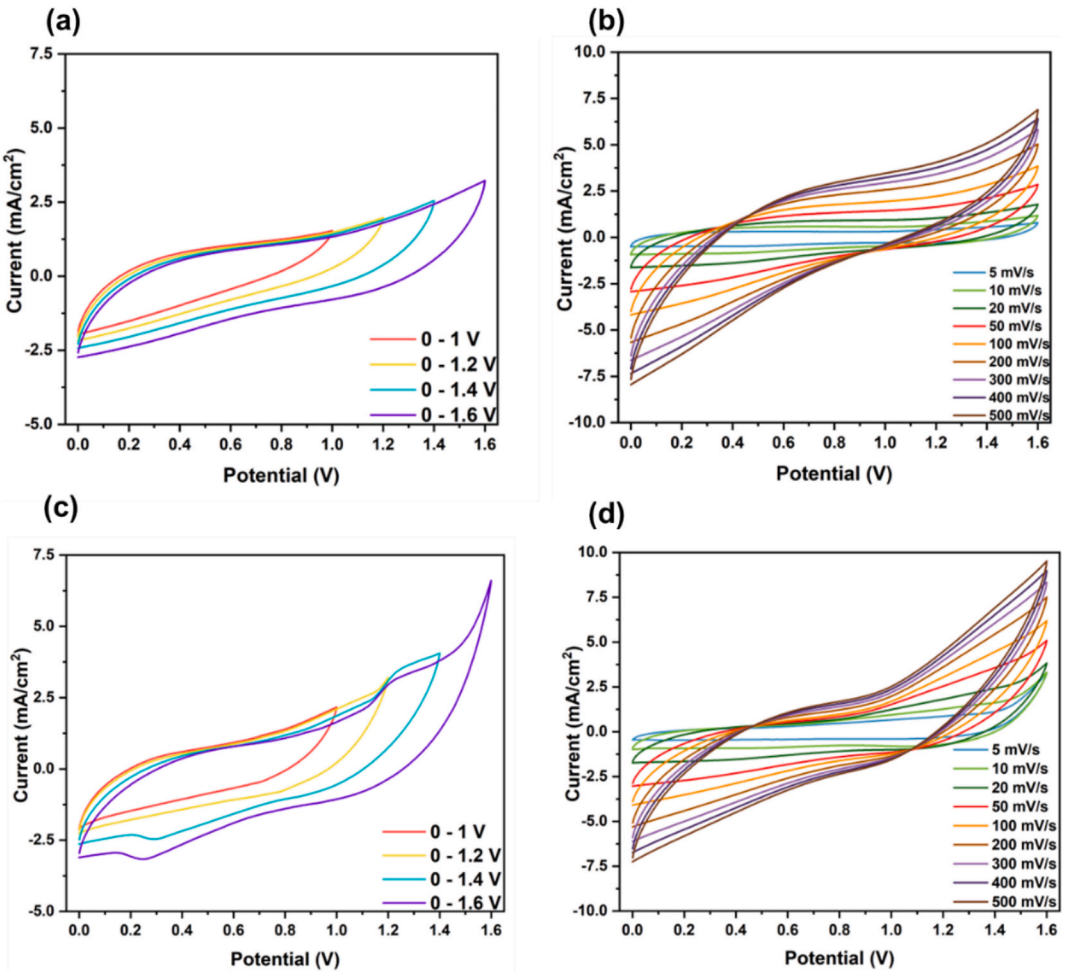


Fig. 11. a) Optimization of the potential range for the CNMO//G supercapacitor, b) Cyclic voltammograms of the CNMO//Gsupercapacitor at different scan rates, c) Optimization of the potential range for the CNMOH//G supercapacitor, d) Cyclic voltammograms of the CNMOH//G supercapacitor at different scan rates.

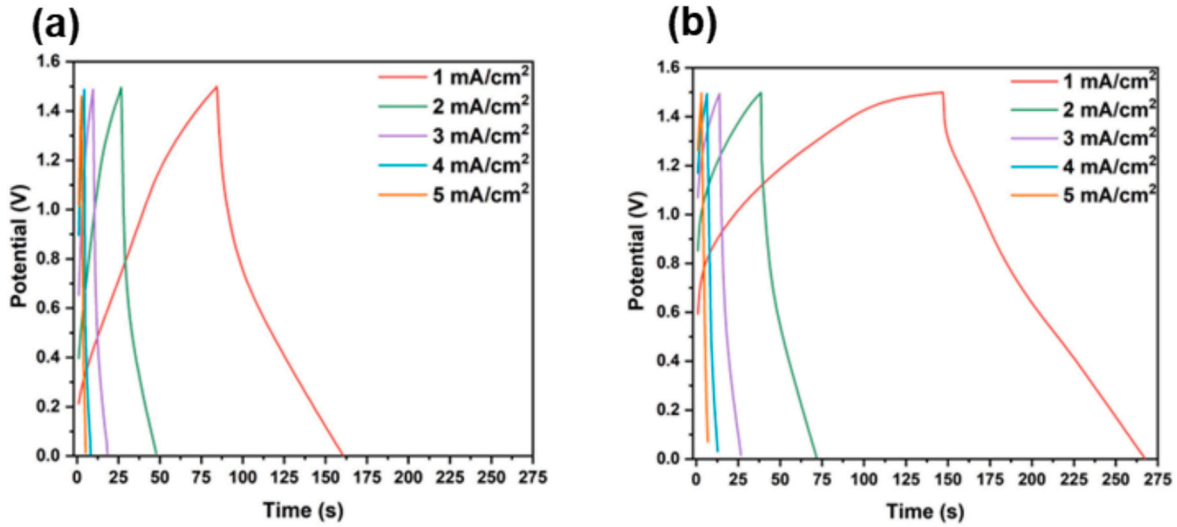


Fig. 12. GDC test of supercapacitors: a) CNMO//G supercapacitor and b) CNMOH//G supercapacitor at different charge–discharge current densities.

hydroxyl groups (O_{OH}), respectively, are shown in Fig. 9d [56].

3.4. Electrochemical measurements

In the electrochemical studies carried out in the three-electrode system, potential range, GCD and CV tests were applied for CNMOH and CNMO electrodes (Fig. 10a-f). Potential range tests were carried out at a scan rate of 50 mV/s and the results are shown in Fig. 10a-b. According to these results, the optimum potential range for both electrodes was found to be −0.2–0.4. Then, cyclic voltammograms of both

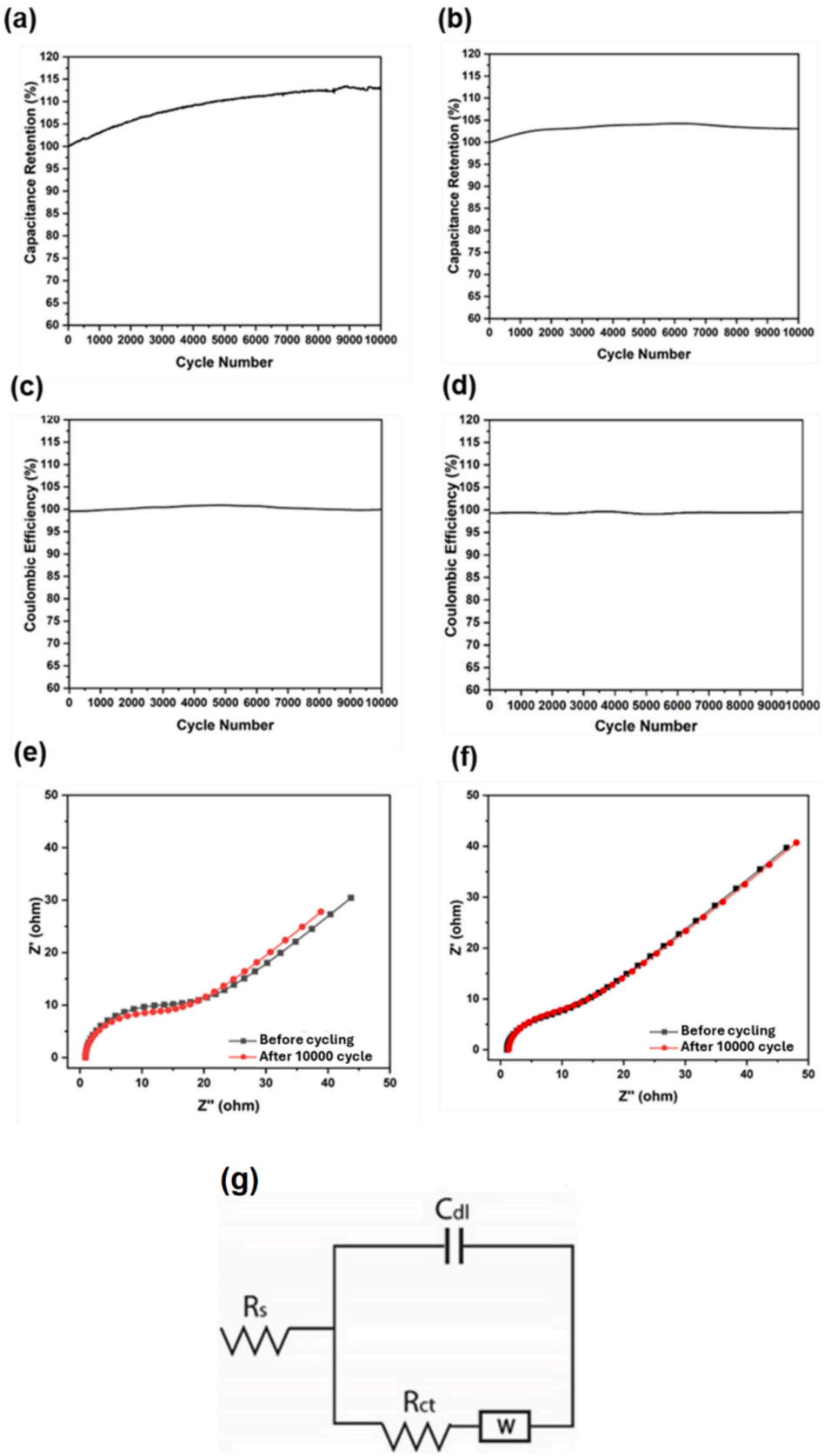


Fig. 13. a) Capacitance retention of the CNMO//G supercapacitor, b) Capacitance retention of the CNMOH//G supercapacitor, c) Coulombic efficiency of the CNMO//G supercapacitor, d) Coulombic efficiency of the CNMOH//G supercapacitor, e) EIS of the CNMO//G supercapacitor before and after 10,000 cycles, f) EIS of the CNMOH//G supercapacitor before and after 10,000 cycles, and g) used equivalent circuit model for fitting of EIS spectra.

Table 3
EIS results of CNMOH//G and CNMO//G supercapacitors (Initial and after 10,000 cycle).

Supercapacitors	Rs (ohm/cm^2)	Rct (ohm/cm^2)	Cdl (mF/cm^2)	W
CNMO//G initial	0.902	1.07×10^{-3}	14,81	3×10^{-2}
CNMO//G after 10,000 cycles	0.891	1.21×10^{-3}	12,4	3.28×10^{-2}
CNMOH//G initial	1,064	8.59×10^{-4}	8,003	2.26×10^{-2}
CNMOH//G after 10,000 cycles	1,295	8.90×10^{-4}	8,597	2.21×10^{-2}

electrodes were taken at a scan rate of 5–500 mV/s (Fig. 10c–d) and the areal capacitance values of CNMOH and CNMO electrodes were determined as 1219 mF/cm^2 and 333 mF/cm^2, respectively, at a scan rate of 5 mV/s. The GCD test results are shown in Fig. 10e-f and the areal capacitance values were calculated as 621.9 mF/cm^2 at a current density of 15 mA/cm^2 in the CNMOH electrode. In CNMO electrode, the areal capacitance value was found as 181.4 mF/cm^2 at a current density of 7.5 mA/cm^2. These results showed that the supercapacitive performances of Co, Ni and Mn in the hydroxide structure were better. Similarly, Zhu et al. found that the supercapacitor performance of $Ni(OH)_2$ was much higher NiO in the supercapacitor test in the three-electrode system with $Ni(OH)_2$ and NiO [57].

Electrochemical tests of the produced supercapacitor devices were performed using CV, GCD, EIS, and long-cycle charge–discharge tests. Initially, CV tests were conducted at a fixed scan rate of 50 mV/s to optimize the potential ranges for the supercapacitors (Fig. 11a and Fig. 11c) and potential range of graphite, CNMOH and CNMO electrodes are also shown in Fig. S3. Cyclic voltammograms were recorded at various scan rates ranging from 5 to 500 mV/s within the determined potential range of 0 to 1.6 V (Fig. 11b and d). The CV results demonstrated that the peak currents increased nearly linearly with the scan rate in all systems under study, indicating that the mass transfer process was predominantly diffusion-controlled [20]. Furthermore, as the scan rate increased, the capacitance decreased due to poor electrolyte–electrode material interaction and the hindered diffusion of electrolyte ions into the electrode's internal structure and pores, a phenomenon commonly referred to as "diffusion limitation" [19,58,59]. In contrast to electric double-layer capacitance, which typically produces a nearly rectangular cyclic voltammogram, the CV profiles in this study displayed a pseudo-rectangular shape, characteristic of pseudocapacitive behavior [60]. This indicates that the capacitance is primarily derived from fast, reversible redox reactions occurring at the surface of the electrode material, which is typical for pseudocapacitive materials. The redox reactions that occur during the oxidation and reduction peaks (which contribute to the pseudocapacitive effect) are generally described by the following equations for $Co(OH)_2$ (eq. (5) and eq. (6) and Co_3O_4 (eq. (7) and eq. (8) [61,62].

$$Co(OH)_2 + OH^- \rightleftharpoons CoOOH + H_2O + e^- \quad (5)$$

$$CoOOH + OH^- \rightleftharpoons CoO_2 + H_2O + e^- \quad (6)$$

$$Co_3O_4 + OH^- + H_2O \rightleftharpoons 3CoOOH + H_2O + e^- \quad (7)$$

$$CoOOH + OH^- \rightleftharpoons CoO_2 + H_2O + e^- \quad (8)$$

In the CV curves of the supercapacitors, the OH^- ion in the electrolyte plays a crucial role in the redox (oxidation–reduction) processes [60]. During the reduction and oxidation processes, OH^- ions are transported from the electrolyte to the electrode surface and vice versa, contributing to the redox peaks observed. The supercapacitors exhibit strong, nearly rectangular-shaped CV profiles with redox activity within the potential range of 0–1.6 V, indicating the successful combination of electric double-layer capacitance (EDLC) with pseudocapacitance [63]. The areal capacitance of the CNMOH//G supercapacitor was determined to be 252 mF/cm^2 at a scan rate of 5 mV/s, based on areal capacitance measurements obtained from CV analysis. Additionally, the specific capacitance of CNMOH//G was found to be 50.8 F/g at the same scan rate. For the CNMO//G supercapacitor, at a scan rate of 5 mV/s, the

Table 4
Comparison of areal capacitance values of this study with results from studies in the literature.

Electrodes compound	Electrode system	Electrolyte	Current density or scan rate	Capacitance	Energy density	Power density	Cyclic stability	Ref.
AC – NiO/rGO	Two-electrode asymmetric supercapacitor	1 M NaOH	0.1 A/g	20.1F/g	40.2 Wh/kg	1440 W/kg	60 % after 200 cycles	[69]
Co_3O_4/CB//GP	Two-electrode asymmetric supercapacitor	6 M KOH	10 mV/s	98 mF/cm^2	–	–	>100 % After 1000 cycles	[19]
Co_3O_4/CB//GP	Two-electrode asymmetric supercapacitor	6 M KOH	1 mA/cm	62 mF/cm^2	22 μWh/cm^2	840 μWh/cm^2	–	[19]
LiNiMnCo-oxide/C76//Graphene	Two-electrode asymmetric supercapacitor	1 M KOH	1 A/g	30 F/g	10 Wh/kg	800 W/kg	115 % after 20,000 cycles	[9]
$Ni_{0.45}Mn_{0.31}Co_{0.24}C_2O_4$//YP-50F Carbon	Two-electrode asymmetric supercapacitor	3 M KOH	0.5 A/g	89,5F/g	36 Wh/kg	118 W/kg	74 % after5000 cycles	[10]
Maxwell Technologies Cells – Ultracapacitors	Two-electrode symmetric supercapacitor	Organic	–	3000F	6.9 Wh/kg	12.3 kW/kg	1,000,000 cycles	[70]
CNMOH//G	Two-electrode asymmetric supercapacitor	6 M KOH	5 mV/s	252 mF/cm^2 50.8F/g	–	–	–	This work
CNMOH//G	Two-electrode asymmetric supercapacitor	6 M KOH	1 mA/cm^2	28.11F/g	8.78 Wh/kg	263.09 W/kg	>100 % After 10,000 cycles	This work
CNMO//G	Two-electrode asymmetric supercapacitor	6 M KOH	5 mV/s	223.17 mF/cm^2 50F/g	–	–	–	This work
CNMO//G	Two-electrode asymmetric supercapacitor	6 M KOH	1 mA/cm^2	22.4F/g	7 Wh/kg	334.35 W/kg	>100 % After 10,000 cycles	This work

areal capacitance was determined to be 223.17 mF/cm^2, while the specific capacitance was 50 F/g. These results highlight the distinct electrochemical performance of the CNMOH//G and CNMO//G supercapacitors, with the CNMOH//G supercapacitor exhibiting higher areal capacitance, which is indicative of superior energy storage capability due to the enhanced pseudocapacitive contribution from the metal hydroxide species.

The GCD) behaviors of the supercapacitors at different current densities are shown in Fig. 12a and b. The results indicate that the shape of the discharge curves does not exclusively correspond to the characteristics of a pure electric double-layer capacitor (EDLC) [60]. This suggests the presence of pseudocapacitance in the materials, contributing to the overall electrochemical performance. At a current density of 1 mA/cm^2, the specific capacitances of the supercapacitors were determined to be 28.11 F/g for the CNMOH//G supercapacitor and 22.4 F/g for the CNMO//G supercapacitor. These values reflect the charge storage capacity of the devices, with the CNMOH//G supercapacitor showing slightly superior performance. In terms of energy and power density, the CNMOH//G supercapacitor exhibited an energy density of 8.78 Wh/kg and a power density of 263.09 W/kg. These values highlight the balance between energy storage and rapid discharge capability. On the other hand, the CNMO//G supercapacitor demonstrated an energy density of 7 Wh/kg and a higher power density of 334.35 W/kg, indicating its ability to deliver power more efficiently, although with a slightly lower energy storage capacity compared to CNMOH//G. These results underscore the distinct advantages of both supercapacitors, with CNMOH//G offering higher energy density and CNMO//G providing higher power density, making them suitable for different applications based on energy storage and power delivery needs.

Long-cycle charge–discharge tests were conducted for 10,000 cycles at a current density of 5 mA/cm^2 to evaluate the cyclic stability of the produced supercapacitors. The capacitance retention of CNMO//G and CNMOH//G supercapacitors over 10,000 cycles is shown in Fig. 13a–b. Both supercapacitors maintained their initial specific capacitance above 100 % and exhibited exceptional electrochemical stability after 10,000 cycles. These results demonstrate that the electrochemical activity of each supercapacitor was highly reversible. A slight increase in capacitance observed could likely be attributed to electrode self-activation, which suggests that more active regions of the electrodes become involved in the electrochemical processes when the electrodes and electrolyte are in optimal contact [64]. Fig. 13c–d illustrates the coulombic efficiency of the supercapacitors over 10,000 cycles. The coulombic efficiencies of both supercapacitors remained close to 100 % throughout the entire cycling period, indicating excellent charge–discharge reversibility.

EIS analyses were performed at open-circuit potential within the frequency range of 10,000 Hz to 0.1 Hz, using an AC voltage with an amplitude of 10 mV to gain a more detailed understanding of the electrochemical characteristics. The EIS results were fitted using the model shown in Fig. 13. Fitted EIS graphs for both CNMO//G and CNMOH//G supercapacitors, before and after 10,000 cycles, are displayed in Fig. 13e–f. Comparison of the EIS spectra after 10,000 cycles with the initial spectra reveals no significant changes, which is consistent with the results of the long-cycle tests. Additionally, numerical EIS data are provided in Table 3. Solution resistance (Rs), which accounts for both the intrinsic electrode resistance and the contact resistance at the electrolyte/electrode interface, is represented by the x-axis intercept in the high-frequency region of the EIS data [65]. The Rs values of the supercapacitors were found to be nearly identical both initially and after 10,000 cycles, indicating minimal changes in the intrinsic and contact resistances over the cycling period [66]. According to the data presented in Table 3, the charge transfer resistance (Rct) values at the beginning and after the 10,000th cycle were very similar, suggesting that the electrochemical interface of the electrode material remained stable throughout the cycling process. Double-layer capacitance (Cdl), which develops at the electrolyte–electrode surface interface, is an important parameter that indicates the ability of the material to store charge at the interface [67]. The Warburg resistance (W), which is associated with the diffusion of ions within the electrolyte, also provides critical insights into the ion transport characteristics of the supercapacitor [68]. e data presented in Table 3 show only minimal variations in both the Cdl and W values after 10,000 cycles, further supporting the conclusion that the supercapacitor's electrochemical performance remained stable during prolonged use. These findings are consistent with the capacitance retention results, which showed that the capacitance of the supercapacitors remained almost unchanged after 10,000 cycles. The high electrochemical stability indicated by the Rs, Rct, Cdl, and W values suggests that the supercapacitors are highly durable, with little degradation in their electrochemical characteristics after extended cycling. Table 4 presents a comparison of the results from this study with the capacitance performance data from other studies in the literature, highlighting the excellent performance and long cycle life of the supercapacitors developed in this work.

4. Conclusions

In this study, cobalt, nickel, and manganese from spent Li-ion battery black mass were leached and subsequently precipitated as hydroxides of cobalt, nickel, and manganese, as well as oxide-based compounds, for use in the cathode electrode composition of a coin cell-type asymmetric supercapacitor. After performing the leaching processes under various conditions, the optimal leaching condition was found to be a 3 M H_2SO_4 acid solution containing 10 % H_2O_2 by volume, conducted for 2 h at room temperature with a solid-to-liquid ratio of 1/50. Following the leaching process, cobalt, nickel, and manganese hydroxides (CNMOH) were obtained via precipitation, and CNMO (cobalt, nickel, manganese oxide) was derived by calcining this substance. These materials were then incorporated into the cathode electrode composition, while nano graphite powder was utilized in the negative electrode composition. The areal capacitance values of CNMOH and CNMO electrodes were determined as 1219 mF/cm^2 and 333 mF/cm^2 at a scan rate of 5 mV/s in three electrode system. The areal and spesific capacitance of the CNMOH//G coin-cell asymmetric supercapacitor at a scan rate of 5 mV/s were determined to be 252 mF/cm^2 and 50.8 F/g respectively. The areal and spesific capacitance of the CNMO//G coin-cell asymmetric supercapacitor were also found as 223.17 mF/cm^2 and 50F/g respectively. Additionally, at a current density of 1 mA/cm^2, the energy density of 7 Wh/kg and power density of 334.35 W/kg for CNMO//G supercapacitor and the energy density of 8.78 Wh/kg and power density of 263.09 W/kg for CNMOH//G supercapacitor were calculated. Long-cycle stability tests revealed that after 10,000 cycles, both CNMOH//G and CNMO//G upercapacitors maintained their initial capacitance values, showing retention of more than 100 %. These results highlight the excellent stability and performance of the fabricated supercapacitors.

CRediT authorship contribution statement

Oğuzhan Onar: Methodology, Investigation. **Sezgin Yasa:** Writing – review & editing, Writing – original draft, Supervision, Resources, Methodology, Investigation. **Ozan Aydin:** Methodology, Investigation. **Burak Birol:** Writing – review & editing, Writing – original draft, Supervision, Methodology, Investigation. **Metin Gencten:** Writing – review & editing, Writing – original draft, Supervision, Methodology, Investigation.

Declaration of competing interest

The authors declare that they have no known competing financial interests or personal relationships that could have appeared to influence the work reported in this paper.

Acknowledgements

This study was supported by The Scientific and Technological Research Council of Türkiye (TÜBİTAK) with project code 124M920. M. Gençten gratefully acknowledges TÜBA for the Outstanding Young Scientists Award (GEBİP).

Appendix A. Supplementary data

Supplementary data to this article can be found online at https://doi.org/10.1016/j.seppur.2025.134695.

Data availability

Data will be made available on request.

References

[1] Q. Abbas, R. Raza, I. Shabbir, A.G. Olabi, Heteroatom doped high porosity carbon nanomaterials as electrodes for energy storage in electrochemical capacitors: a review, J. Sci.: Adv. Mater. Devices 4 (2019) 341–352, https://doi.org/10.1016/j.jsamd.2019.07.007.

[2] Z. Zhang, Z. Fang, Y. Li, Y. Huang, Y. Shen, B. Xiong, W. Zhao, X. Li, X. Lang, H. Yang, A review of recovering lithium and cobalt from spent $LiCoO_2$ lithium-ion batteries cathode, ChemistrySelect 8 (2023), https://doi.org/10.1002/slct.202301983.

[3] S. Yasa, O. Aydin, M. Al-Bujasim, B. Birol, M. Gencten, Recycling valuable materials from the cathodes of spent lithium-ion batteries: a comprehensive review, J. Energy Storage 73 (2023) 109073, https://doi.org/10.1016/j.est.2023.109073.

[4] S. Afroze, M.S. Reza, K. Kuterbekov, A. Kabyshev, M.M. Kubenova, K.Z. Bekmyrza, A.K. Azad, Emerging and recycling of Li-Ion batteries to aid in energy storage, a review, Recycling 8 (2023) 48, https://doi.org/10.3390/recycling8030048.

[5] N. Akhmetov, A. Manakhov, A.S. Al-Qasim, Li-Ion Battery cathode recycling: an emerging response to growing metal demand and accumulating battery waste, Electronics 12 (2023) 1152, https://doi.org/10.3390/electronics12051152.

[6] A. Pražanov, J. Kǒ, M. Havl, D. Pilnaj, V. Knap, Pre-recycling material analysis of NMC lithium-ion battery cells from electric vehicles, Crystals 13 (2023) 214, https://doi.org/10.3390/cryst13020214.

[7] S. Chen, X. Zhang, M. Xia, K. Wei, L. Zhang, X. Zhang, Y. Cui, J. Shu, Issues and challenges of layered lithium nickel cobalt manganese oxides for lithium-ion batteries, J. Electroanal. Chem. 895 (2021) 115412, https://doi.org/10.1016/j.jelechem.2021.115412.

[8] K. Davis, G.P. Demopoulos, Sustainability Hydrometallurgical recycling technologies for NMC Li-ion battery cathodes: current industrial practice and new R & D trends †, RSC Sustain. 1 (2023) 1932–1951, https://doi.org/10.1039/d3su00142c.

[9] Y.I. Mesbah, N. Ahmed, M.M. Hasan, N.K. Allam, Optimized extraction of mesoporous nanocomposites from spent Li- ion batteries and their use to construct high-performance supercapacitor devices with ultra-high stability, Mater. Today Chem. 30 (2023) 101521, https://doi.org/10.1016/j.mtchem.2023.101521.

[10] S. Pappu, S. Muduli, N. Katchala, N.R. Tata, S.V. Bulusu, S.K. Martha, Easy and scalable synthesis of NiMnCo-oxalate electrode material for supercapacitors from spent Li-Ion batteries: power source for electrochromic devices, Energy Fuel 36 (2022) 13398–13407, https://doi.org/10.1021/acs.energyfuels.2c03006.

[11] C. Wei-sheng, H. Hsing-Jung, Recovery of valuable metals from lithium-ion batteries NMC cathode waste materials by hydrometallurgical methods, Metals (Basel) 8 (2018) 321, https://doi.org/10.3390/met8050321.

[12] S. Kim, D. Yang, K. Rhee, Recycling process of spent battery modules in used hybrid electric vehicles using physical/chemical treatments, Res. Chem. Intermed. 40 (2014) 2447–2456, https://doi.org/10.1007/s11164-014-1653-2.

[13] P. Benjamasutin, R. Promphan, P. Hellstr, M. Paulsson, M. Petranikova, Recycling of lithium-ion batteries: effect of hydrogen peroxide and a dosing method on the leaching of LCO, NMC oxides, and industrial black mass, ACS Sustain. Chem. Eng. 11 (2023) 9662–9673, https://doi.org/10.1021/acssuschemeng.3c01238.

[14] H. Nadimi, N.J. Karazmoudeh, Leaching of Co, Mn and Ni using H_2O_2 in sulfuric acid medium from mobile phone LIB, J. Inst. Eng. Ser. D 101 (2020) 111–116, https://doi.org/10.1007/s40033-020-00221-6.

[15] C. Kyoung, K. Rhee, Reductive leaching of cathodic active materials from lithium ion battery wastes, Hydrometallurgy 68 (2003) 5–10, https://doi.org/10.1016/S0304-386X(02)00167-6.

[16] Y. Shen, Z. Yang, H. Lv, J. Ye, K. Sun, J. Pang, L. Chen, One-pot synthesis of CoxSy nanomaterials for high-performance supercapacitors, J. Mater. Sci. Mater. Electron. 33 (2022) 10013–10020, https://doi.org/10.1007/s10854-022-07992-6.

[17] J. Rehman, K. Eid, R. Ali, X. Fan, G. Murtaza, M. Faizan, A. Laref, W. Zheng, R. S. Varma, Engineering of transition metal sulfide nanostructures as efficient electrodes for high-performance supercapacitors, ACS Appl. Energy Mater. 5 (2022) 6481–6498, https://doi.org/10.1021/acsaem.1c03937.

[18] J. Choi, J. Kim, S. Kim, Y. Yun, Simple, green organic acid-based hydrometallurgy for waste-to-energy storage devices: recovery of $NiMnCoC_2O_4$ as an electrode material for pseudocapacitor from spent $LiNiMnCoO_2$ batterie, J. Hazard. Mater. 424 (2022) 127481, https://doi.org/10.1016/j.jhazmat.2021.127481.

[19] S. Yasa, B. Birol, K.B. Donmez, M. Gencten, Recovery of cobalt based materials from spent Li-ion batteries and their use as electrode material for supercapacitor, J. Energy Storage 81 (2024) 110291, https://doi.org/10.1016/j.est.2023.110291.

[20] S. Yasa, B. Birol, M. Gencten, Recovery of cobalt as CoS from spent Li-ion batteries and investigation of its use as an electrode material for supercapacitors, New J. Chem. 47 (2023) 6224–6234, https://doi.org/10.1039/d3nj00380a.

[21] H. Chen, X. Zhu, Y. Chang, J. Cai, R. Zhao, 3D flower-like CoS hierarchitectures recycled from spent $LiCoO_2$ batteries and its application in electrochemical capacitor, Mater. Lett. 218 (2018) 40–43, https://doi.org/10.1016/j.matlet.2018.01.144.

[22] Y. Mao, X. Shen, Z. Wu, L. Zhu, G. Liao, Preparation of Co_3O_4 hollow microspheres by recycling spent lithium- ion batteries and their application in electrochemical supercapacitors, J. Alloys Compd. 816 (2020) 152604, https://doi.org/10.1016/j.jallcom.2019.152604.

[23] V.M. Kumar, S.R. Polaki, R. Krishnan, R.M. Sarguna, T. Mathews, Binder-free vertical graphene nanosheets templated NiO petals for high-performance supercapacitor applications, J. Alloys Compd. 931 (2023) 167420, https://doi.org/10.1016/j.jallcom.2022.167420.

[24] B. Ranjan, G.K. Sharma, D. Kaur, Rationally synthesized Mo_2N nanopyramids for high-performance flexible supercapacitive electrodes with deep insight into the Na-ion storage mechanism, Appl. Surf. Sci. 588 (2022) 152925, https://doi.org/10.1016/j.apsusc.2022.152925.

[25] B. Ranjan, D. Kaur, Pseudocapacitive storage in molybdenum oxynitride nanostructures reactively sputtered on stainless-steel mesh towards an all-solid-state flexible supercapacitor, Small 20 (2024) 1–17, https://doi.org/10.1002/smll.202307723.

[26] O. Aydin, B. Birol, M. Gencten, Production of ZnS based supercapacitor electrode material from ferrochrome ash waste, Ionics (Kiel) 29 (2023) 3335–3352, https://doi.org/10.1007/s11581-023-05018-7.

[27] S. Li, P. Cheng, J. Luo, D. Zhou, W. Xu, J. Li, R. Li, D. Yuan, High-performance flexible asymmetric supercapacitor based on CoAl-LDH and rGO electrodes, Nano-Micro Lett. 9 (2017) 31, https://doi.org/10.1007/s40820-017-0134-8.

[28] D. Chen, S. Rao, D. Wang, H. Cao, W. Xie, Z. Liu, Synergistic leaching of valuable metals from spent Li-ion batteries using sulfuric acid- l-ascorbic acid system, Chem. Eng. J. 388 (2020) 124321, https://doi.org/10.1016/j.cej.2020.124321.

[29] M.A. Hasan, R. Hossain, V. Sahajwalla, Sustainable regeneration of cathode active materials from spent lithium-ion batteries by repurposing waste coffee powder, Green Chem. 27 (2025) 1073–1088, https://doi.org/10.1039/D4GC05048G.

[30] N. Conte, J.M. Gómez, Improving the sorption properties of mesoporous carbons for the removal of cobalt, nickel and manganese from spent lithium-ion batteries effluent, Sep. Purif. Technol. 328 (2024) 125095, https://doi.org/10.1016/j.seppur.2023.125095.

[31] D. Chu, X. Zhao, B. Xiao, A. Libanori, Y. Zhou, L. Tan, H. Ma, H. Pang, X. Wang, Y. Jiang, J. Chen, Nickel/cobalt molybdate hollow rods induced by structure and defect engineering as exceptional electrode materials for hybrid supercapacitor, Chem. – A Eur. J. 27 (2021) 8337–8343, https://doi.org/10.1002/chem.202100265.

[32] B. Liu, S. Sun, R. Jia, H. Zhang, X. Zhu, C. Zhang, J. Xu, T. Zhai, H. Xia, Oxygen-deficient homo-interface toward exciting boost of pseudocapacitance, Adv. Funct. Mater. 30 (2020), https://doi.org/10.1002/adfm.201909546.

[33] C. Zhan, D. Jiang, Understanding the pseudocapacitance of RuO_2 from joint density functional theory, J. Phys. Condens. Matter 28 (2016) 464004, https://doi.org/10.1088/0953-8984/28/46/464004.

[34] Y. Zhang, R. Xu, Z. Qin, S. Feng, W. Wang, C. Chen, A. Ju, Facile preparation of porous sheet–sheet hierarchical nanostructure NiO/Ni–Co–Mn–O x with enhanced specific capacity and cycling stability for high performance supercapacitors, RSC Adv. 10 (2020) 22422–22431, https://doi.org/10.1039/D0RA03056B.

[35] K.A. Abdullin, M.T. Gabdullin, Z.K. Kalkozova, S.T. Nurbolat, M. Mirzaeian, Efficient recovery annealing of the pseudocapacitive electrode with a high loading of cobalt oxide nanoparticles for hybrid supercapacitor applications, Nanomaterials 12 (2022) 3669, https://doi.org/10.3390/nano12203669.

[36] A. Liu, N. Zhang, J. Li, T. Casagrande, C. Butcher, J. Martinez, A. Korinek, G. Botton, J.R. Dahn, Investigating the removal of layered double hydroxides in $[Ni_{0.80}\ Co_{0.15}\ ]_{0.95-x}\ Al_{0.05+x}\ (OH)_2$ (x = 0, 0.05) prepared by coprecipitation, J. Electrochem. Soc. 165 (2018) A2781–A2791, https://doi.org/10.1149/2.0731811jes.

[37] W. Ben Mbarek, M. Al Harbi, B. Hammami, M. Khitouni, L. Escoda, J.-J. Suñol, Nanostructured Mn–Ni powders produced by high-energy ball-milling for water decontamination from RB5 dye, Crystals 13 (2023) 879, https://doi.org/10.3390/cryst13060879.

[38] E.F. Zeid, F.M. Obiedallah, A.-H. Abu-Sehly, W.A.A. Mohamed, M.A. El-Aal, A comparative study of single and bi-doped Co_3O_4 nanocatalysts for the photodegradation of methyl orange dye, J. Mol. Struct. 1293 (2023) 136203, https://doi.org/10.1016/j.molstruc.2023.136203.

[39] L.B. Varela, F. Fernandes, A. Cavaleiro, A.P. Tschiptschin, NbC-Ni coatings deposited by DC reactive magnetron sputtering: effect of Ni content on mechanical properties, thermal stability and oxidation resistance, Surf. Coatings Technol. 349 (2018) 1018–1031, https://doi.org/10.1016/j.surfcoat.2018.06.068.

[40] A. Biswal, B. Dash, B.C. Tripathy, T. Subbaiah, S.M. Shin, K. Sanjay, B.K. Mishra, Influence of alternative alkali reagents on Fe removal during recovery of Mn as electrolytic manganese dioxide (EMD) from Mn sludge, Hydrometallurgy 140 (2013) 151–162, https://doi.org/10.1016/j.hydromet.2013.10.001.

[41] C.R. Rajith Kumar, V.S. Betageri, G. Nagaraju, G.H. Pujar, B.P. Suma, M.S. Latha, Photocatalytic, nitrite sensing and antibacterial studies of facile bio-synthesized

nickel oxide nanoparticles, J. Sci. Adv. Mater. Devices 5 (2020) 48–55, https://doi.org/10.1016/j.jsamd.2020.02.002.
[42] Y. Wang, C. Hou, X. Lin, H. Jiang, C. Zhang, G. Liu, Dye degradation studies of hausmannite manganese oxide (Mn_3O_4) nanoparticles synthesized by chemical method, Appl. Phys. A Mater. Sci. Process. 127 (2021) 1–7, https://doi.org/10.1007/s00339-021-04428-6.
[43] A. Sajid, J. Tariq, F. Ahmad, M.M. Baig, I.H. Gul, U. Habib, Nanostructured Fe-substituted $NiCo_2O_4$@NiMnCo-LDH ternary composite as an electrode material for high-performance supercapacitors, J. Mater. Sci. 58 (2023) 4882–4900, https://doi.org/10.1007/s10853-023-08336-3.
[44] E.A.A. Aboelazm, G.A.M. Ali, K. Feng Chong, Cobalt oxide supercapacitor electrode recovered from spent lithium-ion battery, chemistry of advanced materials, Chem. Adv. Mater. 3 (4) (2018) 67–74.
[45] M.M. Hussain, M.M. Rahman, A.M. Asiri, Ultrasensitive and selective 4-amino-phenol chemical sensor development based on nickel oxide nanoparticles decorated carbon nanotube nanocomposites for green environment, J. Environ. Sci. (China) 53 (2017) 27–38, https://doi.org/10.1016/j.jes.2016.03.028.
[46] M.R. da Silva Pelissari, E. Archela, C.R.T. Tarley, L.H. Dall'Antonia, Ascorbic acid electrocatalytic activity in different electrolyte solutions using electrodeposited Co $(OH)_2$, Ionics (Kiel) 25 (2019) 1911–1920, https://doi.org/10.1007/s11581-019-02845-5.
[47] A.S. Adekunle, J.A.O. Oyekunle, O.S. Oluwafemi, A.O. Joshua, W.O. Makinde, A. O. Ogunfowokan, M.A. Eleruja, E.E. Ebenso, Comparative catalytic properties of Ni $(OH)_2$ and NiO nanoparticles towards the degradation of nitrite (NO_2^-) and nitric oxide (NO), Int. J. Electrochem. Sci. 9 (2014) 3008–3021.
[48] M. Parastar Gharehlar, S. Sheshmani, F.R. Nikmaram, Z. Doroudi, Synergistic potential in spinel ferrite MFe_2O_4 (M = Co, Ni) nanoparticles-mediated graphene oxide: structural aspects, photocatalytic, and kinetic studies, Sci. Rep. 14 (2024) 4625, https://doi.org/10.1038/s41598-024-55452-4.
[49] T. Zhou, Z. Cao, H. Wang, Z. Gao, L. Li, H. Ma, Y. Zhao, Ultrathin Co–Fe hydroxide nanosheet arrays for improved oxygen evolution during water splitting, RSC Adv. 7 (2017) 22818–22824, https://doi.org/10.1039/C7RA01202K.
[50] Z. Yang, J. Chen, Z. Liang, W. Xie, B. Zhao, L. He, Anodic product-derived Bi-MOF as pre-catalyst for cathodic CO_2 reduction: a novel strategy for paired electrolysis, ChemCatChem 15 (2023), https://doi.org/10.1002/cctc.202201321.
[51] S. Anandan, B. Gnana Sundara Raj, G.-J. Lee, J.J. Wu, Sonochemical synthesis of manganese (II) hydroxide for supercapacitor applications, Mater. Res. Bull. 48 (2013) 3357–3361, https://doi.org/10.1016/j.materresbull.2013.05.021.
[52] G. Fu, X. Kang, Y. Zhang, X. Yang, L. Wang, X.-Z. Fu, J. Zhang, J.-L. Luo, J. Liu, Coordination effect-promoted durable Ni$(OH)_2$ for energy-saving hydrogen evolution from water/methanol Co-electrocatalysis, Nano-Micro Lett. 14 (2022) 200, https://doi.org/10.1007/s40820-022-00940-3.
[53] K.B. Ibrahim, G.P. Darshan, G. Benetti, P. Kumar, E. Rodríguez-Castellón, T. A. Shifa, E. Moretti, A. Vomiero, Enhanced oxygen evolution reaction performance of niobium–cobalt oxide catalysts in acidic and alkaline media, Adv. Sustain. Syst. (2025), https://doi.org/10.1002/adsu.202500385.
[54] U. Shuaib, T. Hussain, R. Ahmad, M. Imranullah, M. Amjad, A. Yasin, I. Shakir, D. J. Kang, Novel synthesis of nickel oxide-copper hexacyanoferrate binary hybrid nanocomposite for high-performance supercapacitor application, J. Solid State Electrochem. 27 (2023) 715–725, https://doi.org/10.1007/s10008-022-05357-x.
[55] D. Han, Y. Shen, Y. Zhao, Y. Pan, J. Wei, Y. Wei, Porously nanostructured MnO/C composites directed from polydopamine as high-performance supercapacitor electrodes, J. Mater. Sci. Mater. Electron. 32 (2021) 5781–5789, https://doi.org/10.1007/s10854-021-05298-7.
[56] R. Li, B. Hu, T. Yu, H. Chen, Y. Wang, S. Song, Insights into correlation among surface-structure-activity of cobalt-derived pre-catalyst for oxygen evolution reaction, Adv. Sci. 7 (2020), https://doi.org/10.1002/advs.201902830.
[57] Y. Zhu, C. Cao, S. Tao, W. Chu, Z. Wu, Y. Li, Ultrathin nickel hydroxide and oxide nanosheets: synthesis, characterizations and excellent supercapacitor performances, Sci. Rep. 4 (2014) 5787, https://doi.org/10.1038/srep05787.
[58] O. Gharbi, M.T.T. Tran, B. Tribollet, M. Turmine, V. Vivier, Revisiting cyclic voltammetry and electrochemical impedance spectroscopy analysis for capacitance measurements, Electrochim. Acta 343 (2020) 136109, https://doi.org/10.1016/j.electacta.2020.136109.
[59] V. Subramanian, H. Zhu, R. Vajtai, P.M. Ajayan, B. Wei, Hydrothermal synthesis and pseudocapacitance properties of MnO_2 nanostructures, J. Phys. Chem. B 109 (2005) 20207–20214, https://doi.org/10.1021/jp0543330.
[60] F. Tao, Y.Q. Zhao, G.Q. Zhang, H.L. Li, Electrochemical characterization on cobalt sulfide for electrochemical supercapacitors, Electrochem. Commun. 9 (2007) 1282–1287, https://doi.org/10.1016/j.elecom.2006.11.022.
[61] M.K. Paliwal, S.K. Meher, Co_3O_4 /$NiCo_2O_4$ perforated nanosheets for high-energy-density all-solid-state asymmetric supercapacitors with extended cyclic stability, ACS Appl. Nano Mater. 3 (2020) 4241–4252, https://doi.org/10.1021/acsanm.0c00419.
[62] R.B. Rakhi, W. Chen, D. Cha, H.N. Alshareef, Substrate dependent self-organization of mesoporous cobalt oxide nanowires with remarkable pseudocapacitance, Nano Lett. 12 (2012) 2559–2567, https://doi.org/10.1021/nl300779a.
[63] K. Subramani, N. Sudhan, R. Divya, M. Sathish, All-solid-state asymmetric supercapacitors based on cobalt hexacyanoferrate-derived CoS and activated carbon, RSC Adv. (2017) 6648–6659, https://doi.org/10.1039/c6ra27331a.
[64] B. Yao, L. Yuan, X. Xiao, J. Zhang, Y. Qi, J. Zhou, J. Zhou, B. Hu, W. Chen, Paper-based solid-state supercapacitors with pencil-drawing graphite/polyaniline networks hybrid electrodes, Nano Energy 2 (2013) 1071–1078, https://doi.org/10.1016/j.nanoen.2013.09.002.
[65] J. Zhu, W. Zhou, Y. Zhou, X. Cheng, J. Yang, Cobalt sulfide/reduced graphene oxide nanocomposite with enhanced performance for supercapacitors, J. Electron. Mater. 48 (2019) 1531–1539, https://doi.org/10.1007/s11664-018-06910-z.
[66] X. Meng, J. Deng, J. Zhu, H. Bi, E. Kan, X. Wang, Cobalt sulfide/graphene composite hydrogel as electrode for high-performance pseudocapacitors, Sci. Rep. 6 (2016) 21717, https://doi.org/10.1038/srep21717.
[67] S.J. Patil, J.H. Kim, D.W. Lee, Graphene-nanosheet wrapped cobalt sulphide as a binder free hybrid electrode for asymmetric solid-state supercapacitor, J. Power Sources 342 (2017) 652–665, https://doi.org/10.1016/j.jpowsour.2016.12.096.
[68] N. He, O. Yildiz, Q. Pan, J. Zhu, X. Zhang, P.D. Bradford, Pyrolytic-carbon coating in carbon nanotube foams for better performance in supercapacitors, J. Power Sources 343 (2017) 492–501, https://doi.org/10.1016/j.jpowsour.2017.01.091.
[69] R.I.M. Vitto, M.T. Natividad, S.T. Palisoc, High-performance and low-cost coin-cell supercapacitors based on waste graphite from spent dry-cell batteries, J. Power Sources 582 (2023) 233547, https://doi.org/10.1016/j.jpowsour.2023.233547.
[70] Maxwell Technologies Cells – Ultracapacitors, 2.7 V 3000F Ultracapacitor Cell, BCAP3000 P270 K04/K05, https://maxwell.com/products/ultracapacitors/downloads/, accessed 9th July 2025.